Journal Name

ARTICLE TYPE

Cite this: DOI: 00.0000/xxxxxxxxxx

Evaluation of the influence of Lithium-Ion battery composition on thermal power generation

Luca Giammichele,*[a] Daniele Colarossi,[a] Valerio D'Alessandro,[a] and Matteo Falone[a]

Received Date
Accepted Date

DOI: 00.0000/xxxxxxxxxx

Lithium-ion batteries are currently the most widely technology used for electric mobility. During their service life, batteries can be subjected to high discharge currents, which increase the temperature of the cells. Therefore, it is essential to properly design the battery thermal management system to keep the batteries in the optimal temperature range and to avoid inefficiencies, reduction of life cycles and thermal runaway. These systems require the knowledge of the battery heat generation as accurate as possible. The purpose of this work is to suggest a methodology to evaluate the heat generation of batteries during discharge and to compare the thermal behavior of three commercial batteries usually adopted in electric vehicles. In particular, LFP, NCA, and NMC batteries were experimentally tested at ambient temperature and under different operating currents, measuring cell voltage and surface temperature. The heat generation was evaluated using a simplified equation and the results were deeply analyzed and discussed. The results show that the NCA cell has the highest heat generation and surface temperature. Also the ratio between the heat generated and the electric energy supplied is higher for NCA, while the NMC cell exhibits the lowest value. The NMC shows the highest energy efficiency among the batteries under investigation. The mean efficiency obtained was 0.8, 0.76, and 0.82, respectively for LFP, NCA, and NMC cell.

Nomenclature

Acronyms

$AAD\%$	Average Absolute Difference percent
$BTMS$	Battery Thermal Management System
$CCCV$	Constant Current Constant Voltage
EHC	Entropic Heat Coefficient
IR	Infrared thermography
LFP	Lithium Iron Phosphate
NCA	Lithium Nickel Cobalt Aluminum Oxide
NMC	Lithium Nickel Cobalt Manganese Oxide
SOC	State of Charge

Symbols

$\dot{Q}_t$	Thermal power $[W]$
$\dot{Q}_{irr}$	Irreversible thermal power $[W]$
$\dot{Q}_{rev}$	Reversible thermal power $[W]$
ε	Emissivity
η	Cell energy efficiency
σ	Stefan-Boltzmann constant $[5.67 \cdot 10^{-8} \ W/m^2K^4]$
A	Area of battery surface $[m^2]$
C	Nominal capacity $[Ah]$
C_p	Mean heat capacity at constant pressure $[J/kgK]$
D	Cell diameter $[mm]$
$E_{el,id}$	Ideal electric energy $[J]$
$E_{el,tot}$	Total electric energy $[J]$
$E_{t,tot}$	Total heat generated $[J]$
H	Cell height $[mm]$
h	Convection heat transfer coefficient $[W/m^2K]$
I	Operating current $[A]$
m	Cell mass $[kg]$

* Corresponding author. E-mail: l.giammichele@staff.univpm.it
[a] Dipartimento di Ingegneria Industriale e Scienze Matematiche, Università Politecnica delle Marche, Via Brecce Bianche 12, 60131 Ancona, Italy.

T	Temperature $[K]$
t	Time $[s]$
T_{amb}	Ambient temperature $[K]$
U_{OC}	Open circuit voltage $[V]$
V	Cell voltage $[V]$
V_{max}	Maximum cell voltage $[V]$
V_{nom}	Nominal cell voltage $[V]$
Vol	Volume of the battery $[m^3]$

1 Introduction

Nowadays energy storage plays an even more important role for the integration of renewable energy sources in our society, as they are called to smooth the peaks of energy demand and to provide for the fluctuations of energy production from renewable sources. Among the available technologies, lithium–ion (Li–ion) batteries are one of the most promising as power storage and supply given their characteristics, namely the high energy density and specific power, light weight, low self-discharge rates, high recyclability, and long cycle life, compared to other rechargeable batteries [1–4]. Over the years, different internal chemists have been developed, each of which with different characteristics. Lithium Iron Phosphate ($LiFePO_4$ or LFP) batteries are known for their high thermal stability and long cycle life. They are often used in applications where safety is a primary concern, such as electric vehicles and energy storage systems. Lithium Manganese Oxide ($LiMn_2O_4$ or $LiMnO_2$) batteries provide good power output and thermal stability. They are commonly found in power tools and medical devices. Lithium Nickel Cobalt Manganese Oxide ($LiNi_xCo_yMn_zO_2$ or NMC) batteries offer a balance between energy density, power output, and cycle life. They are used in a wide range of applications, including electric vehicles and portable electronics [5,6]. Lithium Nickel Cobalt Aluminum Oxide ($LiNi_xCo_yAl_zO_2$ or NCA) batteries are similar to NMC batteries but with the addition of aluminum, which further improves energy density. They are often used in electric vehicles and some high-performance consumer electronics. Lithium Titanate ($Li_4Ti_5O_{12}$ or LTO) batteries are known for their extremely long cycle life, fast charge and discharge capabilities, and high thermal stability. They are commonly used in applications where rapid charging and high-power performances are essential, such as buses, forklifts, and some energy storage systems.

Despite the great improvements during the years, regarding the electrochemical behavior, the thermal management of Li–ion batteries is still subject of studies. The focus is on the ageing both over time and also due to operating conditions, such as the state of charge (SOC), delivered/received current, and operation under extreme temperatures. The latter influence the performance, degradation and lifetime of batteries especially out of their optimal temperature range (20 °C – 40 °C) [7,8]. Accordingly, battery thermal management systems (BTMS) are fundamental to optimize the performances of such batteries.

In addition, it is worth mentioning that batteries, during the daily working, are characterized by a heat generation. An appropriate evaluation of single–cell heat generation improves the BTMS design method. The phenomenon of the heat generation is related to different mechanisms such as ohmic Joule heating due to the transport of charged particles, the start of interfacial processes, and the movement of concentration species [9]. In open literature, two main terms characterize the battery heat generation: irreversible and reversible heat generation. The irreversible term is related to the joule effect due to the battery internal resistance and to the overpotentials at the interface. The reversible heat depends on the entropic heat coefficient (EHC). This parameter is representative of the chemical reaction inside the battery and the electrodes composition. The reversible heat was often neglected [10,11] or considered constant with the SOC [12–14]. However, some studies show how this term can assume the same magnitude of irreversible heat [15–17]. Therefore, it can significantly affect the total heat generation and the cell surface temperature [18].

In literature, different studies deal with the phenomenon numerically [19]. More in detail, some numerical models allow to simulate the heat generation, discretizing the cell in different regions and investigating which are most subject to the phenomenon. For instance, a three-region [19] and seven-region [20] discretization have been proposed. Experimentally the discretization is more complex, and accordingly studies focus on the evaluation of the heat generated by the entire battery. This is crucial as design parameter for the cooling strategy adopted as BTMS. The most common ones are air cooling systems [21,22], both in natural and forced convection, liquid cooling strategies, usually more effective for their high thermal capacities, which exploit a single–phase or two–phase refrigerant [23–25], immersion liquid cooling [26,27], phase change materials [28–30], and heat pipe or pulsating heat pipe [31–33]

This paper intends to provide an extended experimental study of the heat generation of three commercial battery usually adopted in electric vehicles with different chemists, considering the overall thermal behavior of these cells. In fact, the already present studies operate under different test conditions and a comparison can be difficult. For this reason, the aims of the proposed work are:

- to propose a standard methodology for the thermal characterization of cells.
- to provide a comparison of the different chemists in order to create a database. This can be used to select the best chemists and to optimize the BTMS for the specific application.
- the use of the experimental results as validation for the numerical models proposed in literature.

The remainder of this paper is organized as follows. Section 2 describes the heat generation model adopted. The experimental setup is explained in Section 3. Section 4 shows the results of experimental tests. Finally, section 5 is devoted to the evaluation of the cell heat generation. Section 6 contains the conclusions.

2 Battery heat generation model

The overall energy balance can be expressed using Eq. (1), where the thermal energy stored within the cell is equal to the heat generated minus the heat loss by convection and radiation.

$$mC_p\frac{dT}{dt} = \dot{Q}_t - hA(T - T_{amb}) - \varepsilon\sigma A(T^4 - T_{amb}^4) \quad (1)$$

A simplified equation (Eq. 2) of the heat generation model proposed by Bernardi et al.[34] was adopted to evaluate the heat generation of the cells under investigation. This equation is extensively used to calculate Li–ion batteries heat generation[9,11,15,16,35–37].

$$\dot{Q}_t = \underbrace{I\cdot(V - U_{OC})}_{\dot{Q}_{irr}} + \underbrace{I\cdot T\cdot\frac{\partial U_{OC}}{\partial T}}_{\dot{Q}_{rev}} \quad (2)$$

where I is the discharge current, V is the cell voltage, T is the battery temperature, U_{OC} is the open circuit voltage, and $\partial U_{OC}/\partial T$ is the EHC.

The irreversible term depends on the cell overpotential, equal to the difference between V and U_{OC}, and the operating current. The contribution of this term to the total amount of heat generated is always positive because the cell voltage is lower than the U_{OC} during discharge and the current was considered negative in the discharge phase. This term is related to irreversible processes such as Joule heating within the battery, and proportionally depends on the internal resistance of cells.

The reversible term is related to the entropy change in the electrochemical reaction and it is strongly influenced by the EHC. The EHC can be positive or negative and depends on the SOC and chemistry composition. If the EHC is negative, the reversible heat is positive and the process is exothermic; otherwise if the EHC is positive the reversible heat is negative and the process is endothermic.

Eq. (3) represents the total amount of electric energy produced during discharge, where τ is the time required to fully discharge the battery at the operating current, V is the cell voltage, and I is the operating current. Similarly, a total heat generated by the battery can be also defined in Eq. (4).

$$E_{el,tot} = \int_0^\tau V\cdot|I|\,dt \quad (3)$$

$$E_{t,tot} = \int_0^\tau \dot{Q}_t\,dt \quad (4)$$

The cell energy efficiency can be defined in Eq. (5) as the ratio between total electric energy actually produced and the maximum electric energy that the battery can supply without any losses.

$$\eta = \frac{E_{el,tot}}{E_{el,id}} \quad (5)$$

The ideal electric energy, $E_{el,id}$, was calculated as reported in Eq. (6), where V_{max} is the cell voltage at full charge condition, and C is the nominal capacity of the cell.

$$E_{el,id} = V_{max}\cdot C \quad (6)$$

Table 1 Cell characteristics

Cell	D [mm]	H [mm]	m [g]	V_{nom} [V]	V_{max} [V]	C [Ah]
LFP	26	65	76	3.3	3.6	2.5
NMC	21	70	70	3.6	4.2	4.5
NCA	20	70	63	3.6	4.2	4.25

3 Experimental apparatus

Three commercial cylindrical cells commonly adopted in electric vehicles and with different chemical composition were tested: Lithium Iron Phosphate $LiFePO_4$ (LFP), Lithium Nickel Manganese Cobalt Oxide 811 $LiNi_{0.8}Mn_{0.1}Co_{0.1}O_2$ (NMC), and Ni rich Lithium Nickel Cobalt Aluminum Oxide $LiNi_{0.8}Co_{0.15}Al_{0.05}O_2$ (NCA). The LFP cell was a A123 26650 (series name ANR26650M1–B), the NMC was a Molicel 21700 (series name INR-21700-P42B), and the NCA was a Sanyo 20700 (series name NCR20700B). The main characteristics of the cells, as reported in the technical specifications, are summarized in Table 1, where D, H, m, V_{nom}, V_{max}, and C are the diameter, height, weight, nominal voltage, maximum voltage (fully charged), and the capacity of the cells, respectively.

A programmable power supply (RMX–4125) and DC electronic load (RMX–4005) were used to manage the charging and discharging phase. The current setting accuracy of the electronic load is ±0.1% F.S. ranging from 0 to 70 A and a resolution of 2 mA. The voltage of the cells was measured by NI 6289 data acquisition device, which has 0.076 mV of resolution ranging from 0 to 10 V and an uncertainty of ±0.25 mV. The operating current was measured by a current transducer with an uncertainty of ±0.02 A in the range ±85 A. Ambient temperature and relative humidity were measured with an uncertainty of ±0.6 °C and ±2.5%, respectively. Then, the signals of current and ambient parameters were acquired using the NI 6289 data acquisition device.

The temperature of the battery surface was measured by thermocouples. One T–type thermocouple was placed in center of the battery height using a high–conductivity adhesive. The thermocouples were attached to an ice point reference before being acquired by the data logger. A high–precision calibration bath was used to calibrate the thermocouples, allowing to obtain an uncertainty of ±0.06 °C. Infrared thermography was used to evaluate the temperature distribution on cell surface. The infrared camera used is the FLIR A655sc, equipped with a 640x480 micro–bolometric sensor array and a 25° lens with a 25° x 19° field of view. The camera uncertainty is ±2% of the measured value, while the thermal sensitivity is 30 mK at 30 °C. A high emissivity (0.94) black matte paint was applied on battery surface. Figure 1 shows the measurement setup described above.

During the tests, the following parameters were acquired at 25 Hz: cell voltage, operating current, battery temperature (using thermocouples), ambient temperature and relative humidity. Then, the data were post–processed and averaged at 1 Hz. Meanwhile, IR images were also acquired once per second. The thermal camera was placed at a distance of 0.3 m from the battery, resulting in a spatial resolution of 0.2 mm per pixel. Each image obtained during discharge was then subtracted from the reference

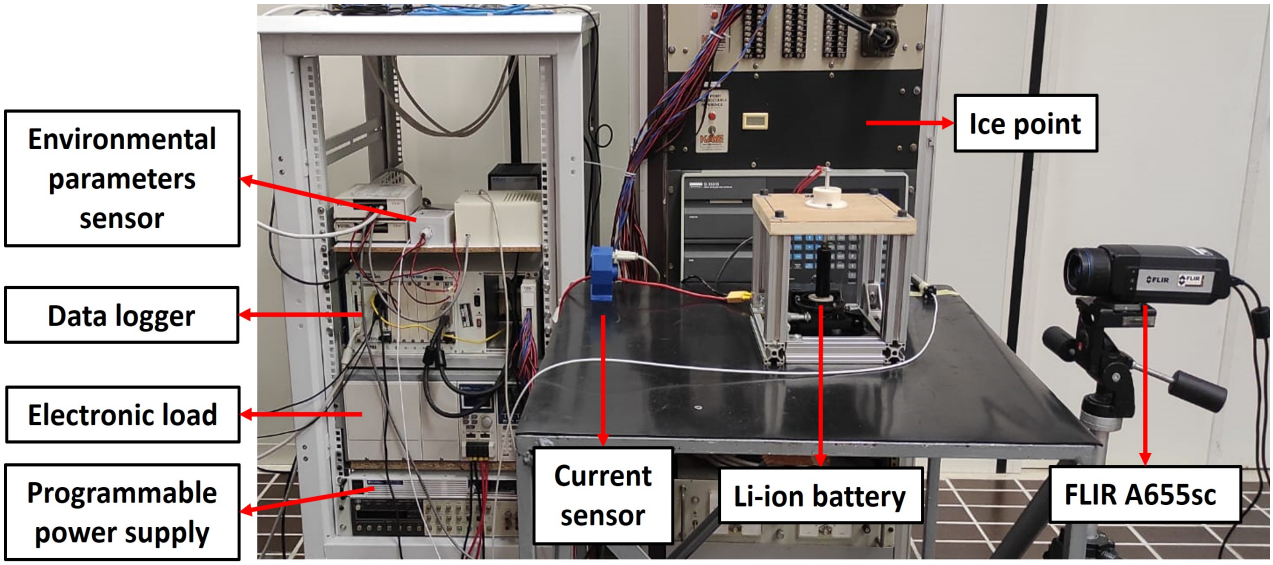

Fig. 1 Experimental setup.

thermal image related to the initial condition. All the tests were performed at ambient temperature (ranging between 26 °C and 28 °C). Thermocouple measurements are referred to their initial value to avoid the influence of environmental temperature variation. The ambient temperature and relative humidity were used in the thermographic image acquisition software as input parameters to perform temperature measurements.

Uncertainty analysis was performed considering both the instrument uncertainty and type random measurement uncertainty. The combined uncertainties were evaluated for correlated quantities (i.e. thermal power generated, total electric energy, and battery efficiency). A coverage factor equal to 2 was considered in the calculation of the expanded uncertainties. The obtained uncertainties are ± 0.3 mV for U_{OC} measurements and maximum 0.3% for the SOC calculation. This last value is due to the setting current accuracy of the electronic load and the measurement uncertainty of the current sensor. In the evaluation of the EHC, we obtained a maximum value of uncertainty equal to ± 0.016 mV/K. The measurement uncertainty of the correlated quantities is summarized in Table 2, where the largest percentage uncertainty for each C–rate is reported. The C–rate is the rate at which a battery is charged or discharged. It is defined as the ratio between the discharge current applied and the discharge current under which the battery delivers its nominal capacity per hour.

Table 2 Measurement uncertainty

C-rate	1	2	3	4	5
$\dot{Q}_t$%	$\pm$ 5.18	$\pm$ 2.15	$\pm$ 0.63	$\pm$ 0.72	$\pm$ 0.6
$E_{el,tot}$%	$\pm$ 5.2	$\pm$ 2.68	$\pm$ 0.68	$\pm$ 0.62	$\pm$ 0.58
η%	$\pm$ 1.64	$\pm$ 0.85	$\pm$ 0.22	$\pm$ 0.19	$\pm$ 0.18

4 Experimental results

Three kinds of experimental tests were performed in order to calculate the thermal power generated using Eq. (2). First of all, it was necessary to measure the U_{OC} and the EHC coefficient for the chemistry under investigation. Then, constant current discharge tests were performed to obtain the cell voltage and the battery surface temperature under different operating currents.

4.1 Open circuit voltage

The test consists in a low current discharge (1C) of 10% of SOC followed by one hour of relaxation. This cycle was repeated each 10% of SOC until the battery was completely discharged. Meanwhile, the cell voltage was acquired at 10 Hz and the mean value of the last 10 minutes of each relaxation time was considered a stable value of U_{OC}. The U_{OC} test was repeated three times for each chemistry. The following figure refers to the mean value of the three tests and the average absolute difference percent, AAD%, was used to quantify the measurement repeatability. This parameter is defined by the following equation:

$$AAD\% = \frac{100}{N_{exp}} \sum_{i=1}^{N_{exp}} \left| \frac{X_i^{(exp)} - X_i^{(num)}}{X_i^{(num)}} \right| \tag{7}$$

where N_{exp} is the number of experimental data and X is a generic parameter. The AAD% was equal to 0.18, 0.24, and 0.72, respectively for the LFP, NCA, and NMC batteries. The results are showed in Figure 2.

NMC and NCA cells exhibit an higher value of U_{OC} for all the SOC. LFP cell has a plateux between 90% and 10%. Then there is a rapid fall to the minimum voltage. On the contrary, NMC and NCA cells have a gradual decrease of U_{OC} without a range of constant values. Furthermore, the decrease is more rapid for the NMC.

4.2 Entropic Heat Coefficient

The EHC was measured through potentiometric methods, which are extensively applied in literature[15,16,35,36,38]. The cells were placed in a high precision thermostatic bath after discharged to a specific SOC. After a period of relaxation of three hours, the bat-

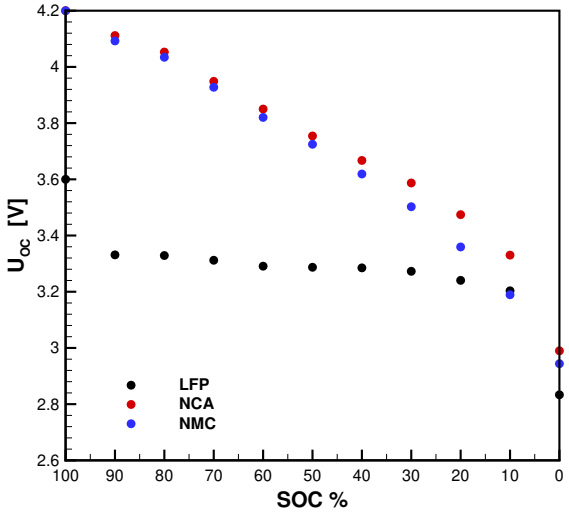

Fig. 2 Open circuit voltage as a function of SOC.

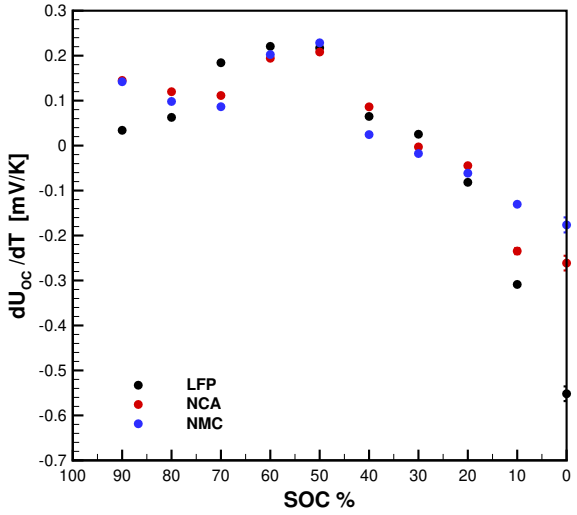

Fig. 3 EHC as a function of SOC.

tery was subjected to a thermal cycle consisting in five temperature steps spaced out by three hours of relaxation at the corresponding temperature. The temperature steps used in this study were 25 °C, 10 °C, 35 °C, 45 °C, and 25 °C. Meanwhile, the cell voltage and surface temperature were acquired at 10 Hz. The mean value of the last 10 minutes of each relaxation time was considered stable U_{OC} at the corresponding bath temperature. These values were plotted against the temperature and a linear interpolation was applied. The slope of the curve represents the EHC. This procedure was repeated every 10% of SOC until the cell was completely discharged. The results are showed in Figure 3.

The trend is quite similar for the three cells: the maximum positive value is between 60% and 50% of SOC and the EHC assumes positive values until the 40%, is nearly zeros at 30%, and becomes negative for the rest of the SOC. The reversible heat is negative when the EHC is positive. In this case the chemical reactions inside the battery are endothermic and the total heat generated is decreased by the reversible part. Otherwise, a negative value of EHC leads to a positive reversible heat. In this case the total heat generated is increased by this term. However, there are same significant differences at high and low SOCs. Between 100% and 70% the NMC and NCA cells exhibit a decreasing trend, while the EHC increases for the LFP. Furthermore, at low SOCs the EHC decreases for all the chemists but more for the LFP and NCA than for the NMC. Consequently, also the heat generation at these SOCs will be higher due to the higher contribution of positive reversible heat.

4.3 Constant current discharges

Constant current discharge tests were performed to measure the last parameters necessary to evaluate the heat generation (i.e. cell voltage, surface temperature, and actual current applied). The tests were performed at different operating currents, as reported in Table 3. For the NCA cell was not possible to test also the 5C case because the datasheet recommends to not exceed a constant current discharge equal to 4C.

Table 3 Constant current discharge tests performed

C-rate	1	2	3	4	5
Current LFP [A]	2.5	5	7.5	10	12.5
Current NCA [A]	4.25	8.5	12.75	17	-
Current NMC [A]	4.5	9	13.5	18	22.5
Time [s]	3600	1800	1200	900	720

The cells were completely discharged until reaching their minimum voltage, equal to 2 V and 2.5 V, respectively for LFP and NMC/NCA cells. For the NCA test at 4C, the discharge was ended before reaching the minimum voltage level because the cell surface temperature was approaching 100 °C and the test was stopped for safety reasons. After the complete discharge, the cells were charged applying a standard CCCV charge (Constant Current Constant Voltage). During the test, cell voltage, surface temperature, current supplied, ambient temperature and ambient relative humidity were measured. The results are showed in the following figures (Figures 4-6).

Figure 4 shows both the cell voltage during discharge and U_{OC} against the SOC for the three batteries under investigation. As already discussed for the U_{OC}, the cell voltage of LFP exhibits a plateau between 90% and 10% of SOC, while the other two cells have a gradual decrease of voltage. However, the LFP shows a rapid decrease of voltage in the last 20% of SOC. It is worth noting that the almost flat operating voltage between 90% and 10% of SOC (as well as the U_{OC} trend of figure 2) is a typical behavior of this kind of chemist. From the figure, the decrease of cell voltage due to the current supplied by the battery is immediately evident: the cell voltage during discharge is lower than the U_{OC} for all the SOC and the difference increases with the discharge current. This difference is due to the internal resistance of the cell and it is directly involved in the irreversible heat generation term of Eq. (2): a higher value of this difference corresponds to a higher irreversible heat generation (at the same discharge current) and a greater increase of the surface temperature. Figure

4 also highlights that the NCA cell has the highest cell voltage decrease with respect to the U_{OC}, while the NMC has the lowest one. Furthermore, the decrease of the voltage within the discharge current is also more marked. Consequently, the temperature increases and the heat generation will be higher for this cell at the same discharge current.

Figure 5 shows the difference between the cell surface temperature during the discharge phase and its initial value. During the discharge phase the temperature increases due to the heat generation and the increase is more evident for higher operating currents. According to the behavior shown in Figure 4, the NCA cell reaches the highest temperature at the end of discharge. The LFP has the lowest temperature rise between the cells that could seems discorded with what explained before. However, the increase of temperature during the discharge is related to the cell overpotential and the operating current, considering the irreversible term of Eq. (2). This cell has a lower capacity than the other two and the operating current is lower for the same C-rate. In this case, the higher cell overpotential (with regards to the NMC) is balanced by the lower operating current and the temperature rise is lower. Otherwise, the effect of the higher cell overpotential is clearly visible comparing the NMC and NCA temperature plot. Indeed, at almost equal discharge current, the NCA exhibits a higher temperature increase due to the higher cell overpotential.

Another interesting aspect to analyze is the behavior of the 1C discharge. The temperature has a first rise when the discharge starts. Then, at about 60% of SOC there is a change of curvature, more evident in the LFP than the NCA, while also for the NMC there is a temperature decrease. Finally, at the end of the discharge the temperature rises with a higher slope. This trend is gradually less visible with the increase of the C-rate. The explanation of these results is in the relation between the irreversible and reversible terms of Eq. (2). At low operating currents, it was found that the reversible heat absolute value is comparable with the irreversible term; while at higher C-rates the irreversible term is strongly higher than the reversible one. Furthermore, until the 30% of SOC the reversible heat is of the opposite sign of the irreversible heat. In this area the reversible heat is subtracted to the irreversible one and the temperature increase is lower. At higher C-rates the reversible term has the same behavior, but the irreversible term has a higher impact on the total heat generated. After the 30% of SOC the reversible heat becomes positive and it is added to the irreversible one. Consequently the temperature increases with higher intensity.

Finally, Figure 6 shows the termographic images of the three cells. For compactness, only the 4C discharge was considered, which correspond to the maximum discharge current for the NCA cell. The images were taken every 25% of SOC with the exception of the last SOC value which is equal to 5.5%. This last value corresponds to the end of discharge for the NCA cell that was stopped in advance for safety reasons. The color map refers to the temperature difference between the cell surface temperature and its minimum value. For the NMC cell there is an unevenness on the right edge of the battery due to the precence of the thermocouple and the adhesive adopted for the bonding. The figure highlights

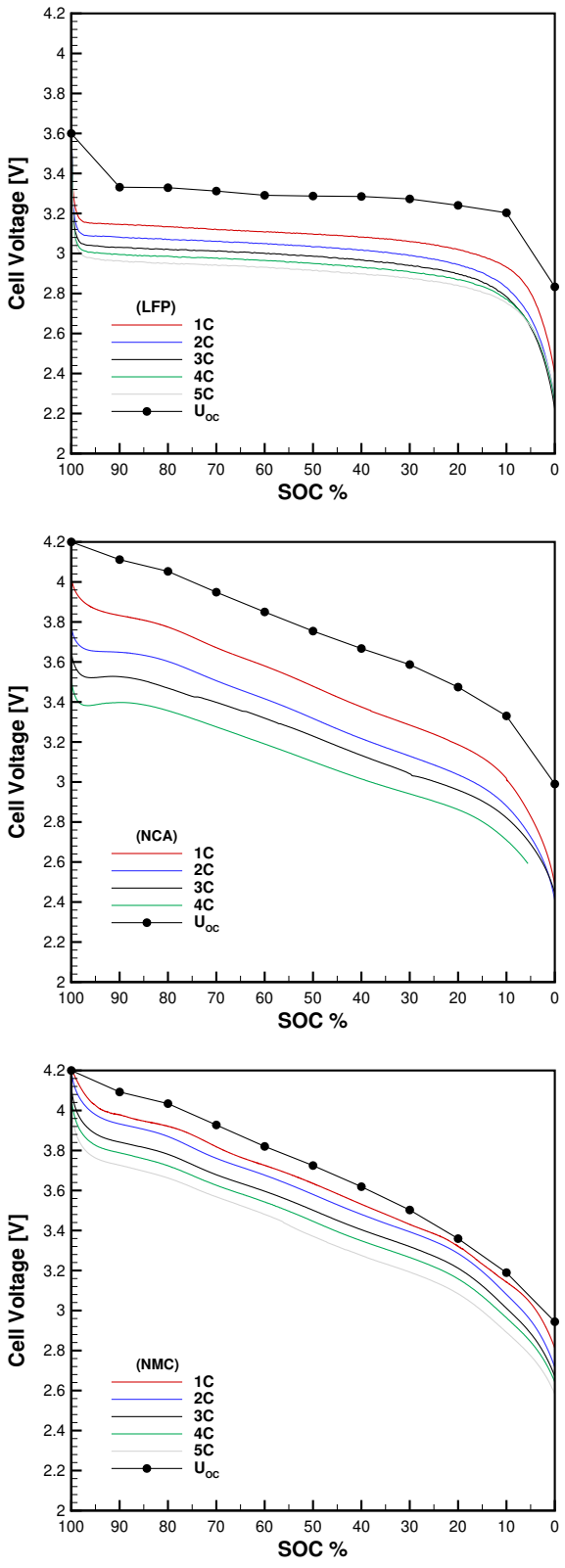

Fig. 4 Cell voltage at various discharge currents.

the temperature distribution over cell surface. For all the cells the higher temperature is located in the top zone and the temperature decreases proceeding towards the bottom part. This distribution

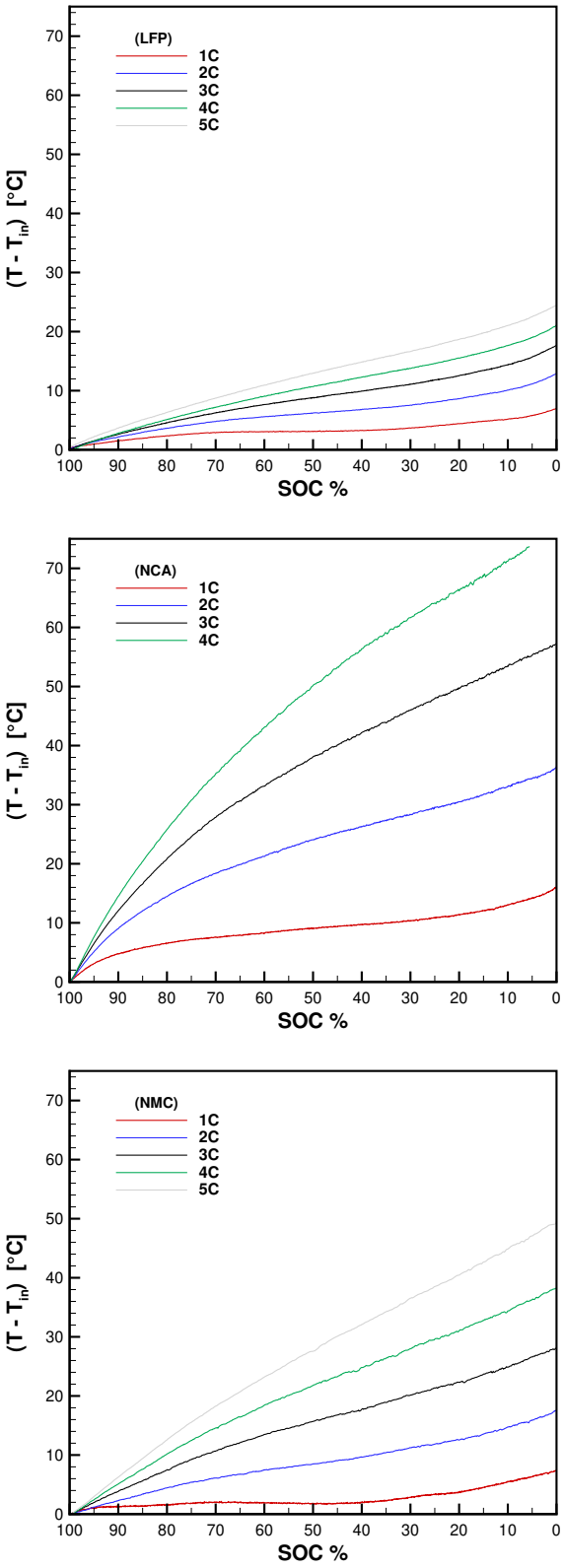

Fig. 5 Surface temperature at various discharge currents.

can be attributed to natural convection on the battery surface. On the bottom side, there is a higher heat transfer due to cold air near the battery surface. Proceeding upwards, the surrounding air is influenced by the surface temperature and increases its temperature. Consequently the heat transfer decreases proceeding upwards. Furthermore, this behavior is influenced by the different tab and current collector materials of the positive and negative poles of the cell. It is also very clear that the NCA cell exhibits a higher temperature difference on cell surface, while the NMC has the greatest temperature uniformity.

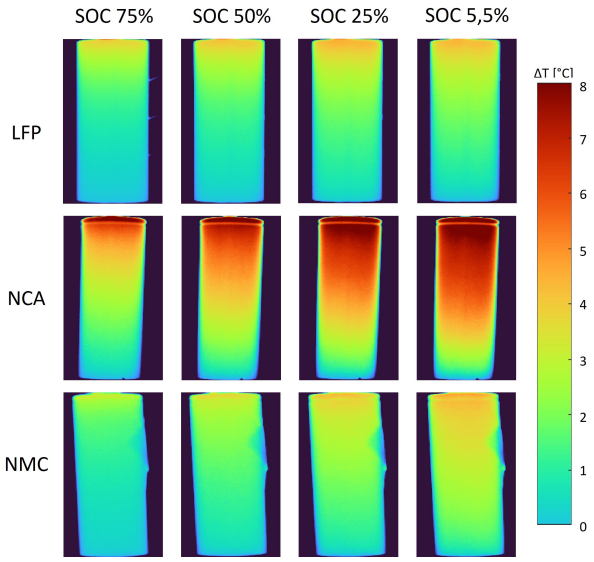

Fig. 6 IR images of the three cells during 4C constant current discharge.

5 Evaluation of heat generated

The experimental results showed in section 4 were used to evaluate the thermal power generated by the batteries using Eq. (2). The thermal power calculated was then divided by the cell volume in order to avoid the influence of different battery size on the results.

Figure 7 shows the volumetric thermal power generated for the three cells calculated every 10% of SOC (in the points where the U_{OC} and EHC were measured) until complete discharge. The last point calculated for the NCA cell was at 10% of SOC for the 4C discharge current, because the test was ended a few seconds after this point for safety reasons.

The volumetric thermal power for all the three cells increases with the discharge current. Until the 20% of SOC the thermal power values fluctuate around a mean value. Differently, the thermal power increases very rapidly in the last 20% of SOC. This behavior is due to the effect of the reversible term of Eq. (2), which becomes positive after the 30% of SOC and is added to the irreversible term. Furthermore, all the cells have the minimum thermal power generated between 60% and 50% of SOC. At these values, it was found that the EHC has its maximum positive value and the reversible heat assumes its maximum negative value (Figure 3).

NCA cell has the highest volumetric thermal power generated at the same C-rate, followed by the NMC and the LFP. The results are in agreement with the surface temperature measurements, where it was found a higher temperature for the NCA cell (Fig-

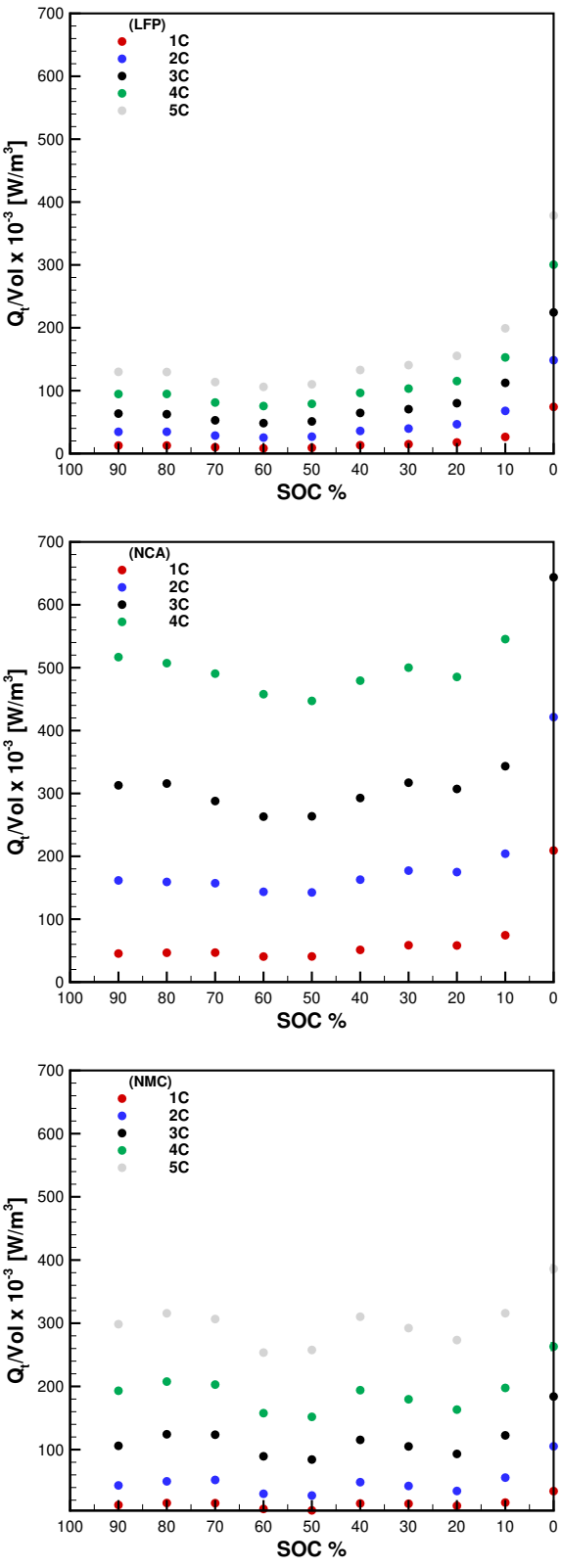

Fig. 7 Volumetric thermal power generated at various discharge currents.

ure 5). The higher thermal power generated is due to the higher cell overpotential, clearly visible in Figure 4. From the figure, the NMC overpotential is lower than the LFP battery, but the heat generated and the surface temperature are higher than the LFP ones. As explained before, this is due to the higher cell capacity and supplied current at the same C-rate. To highlight this behavior, the thermal power generated was divided by the operating current and the results are shown in figure 8. This operation allows a better comparison between the cells avoiding the influences of the different capacity. The highest value is always relative to the NCA cell; however, the NMC exhibits lower values then LFP due to the lower overpotential. Looking at the last 20% of discharge, the thermal power increase is higher for the LFP and NCA cells with respect to the NMC, according to the EHC plot (Figure 3). Indeed, the EHC was found to be lower for NMC cell at the end of discharge. Furthermore, in this range the NMC cell has also the lowest overpotential.

From the above analysis the NMC and NCA cells have a higher volumetric thermal power generation. However, they also could supply a higher electric energy due to the higher cell voltage during discharge and nominal capacity. Considering the total electric energy calculated using Eq. (3) it was found that NMC and the NCA cells supplied the 113% and 83% more than the LFP electric energy, respectively.

Table 4 shows the percentage ratio between the total heat generated and the total electric energy calculated using Eq. (3) and Eq. (4). It is clear that the heat generated is only a limited part of the electric energy for the NMC cell. Otherwise for the other two chemists the heat generated has a higher impact. In particular, the results point out that the NCA cell has the highest ratio and the heat generated is very relevant with respect to the electric energy supplied, for all the C-rate tested.

Table 4 Percentage ratio between total heat generated and total electric energy supplied

C-rate	1	2	3	4	5
LFP	9.74	11.96	13.65	14.88	16.11
NCA	11.06	15.99	19.35	20.94	-
NMC	2.19	3.77	6.07	7.63	9.85

It is worth noting that in this article the heat generated is calculated for the cell as a whole, without going into detail of the contributions due to the different components of the cells. Of course the thermal power generation of a cell is closely related to the chemical composition of the cathode, anode, and electrolyte, but also to the size of the electrodes and the type and size of the current collectors. Therefore, the different thermal behaviors previously discussed are not only attributable to the different chemical composition of the cathode but can also be linked to the differences in other components of the cells.

Finally, Figure 9 shows a comparison between the energy efficiency of the three cells under different operating currents. The efficiency, as defined in Eq. (5), takes into account the inefficiency due to (i) the decrease of U_{OC} with the SOC regards to the maximum voltage at full charge; (ii) the cell overpotential during discharge and the heat generation. The NCA cell has always the worst efficiency due to the very high heat generation. NMC has a higher efficiency than LFP for all the C-rates, even if the values

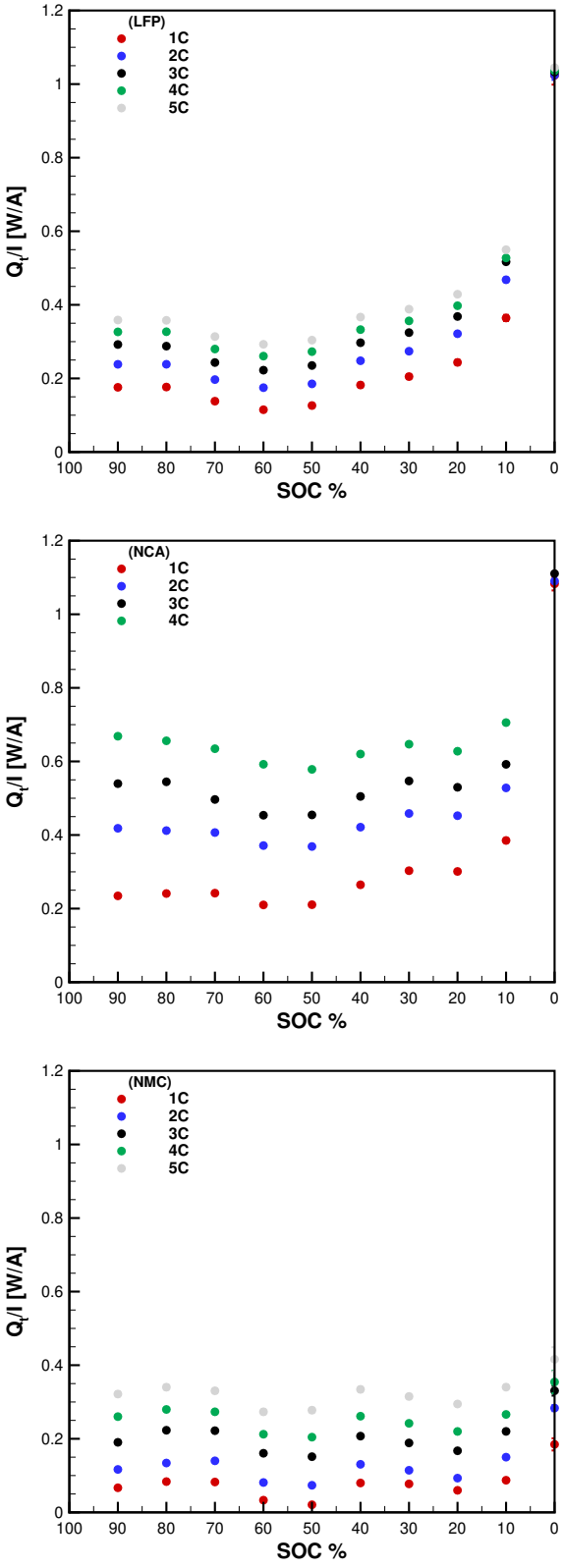

Fig. 8 Thermal power generated normalized on operating current at various discharge currents.

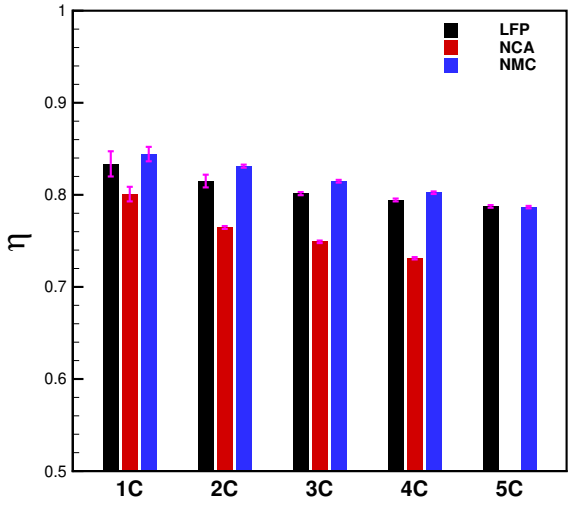

Fig. 9 Comparison of battery energy efficiency at various C-rates.

are quite similar. For the LFP the highest contribution is the inefficiency due to the cell overpotential, significantly higher than the NMC. However, the inefficiency due to the decrease of U_{OC} compared to the maximum voltage is higher for the NMC cell. The relation between the two contributions for NMC and LFP cells can be easily understand looking at Figure 10. The inefficiency due to the cell overpotential and the U_{OC} decrease with SOC are represented by the orange and gray, respectively; while, the green area is the electric energy actually supplied by the battery. The sum of the three areas is the ideal electric energy. The figure immediately points out the contribution of the two inefficiencies. The orange area is greater for the LFP cell than the NMC one due to the higher overpotential. Otherwise, the gray area is more extended for the NMC battery. For the LFP cell, the two inefficiency contributions are similar, while in the NMC cell the U_{OC} decrease is the main contribution. It is also clear that the supplied electric energy (green area) of the NMC cell is significantly higher than the LFP one due to the higher maximum cell voltage.

It is interesting to evaluate the specific electric energy available for the batteries with respect to their weight and volume. The gravimetric energy density and the volumetric energy density are attractive data for electric vehicle battery packs. For example, for drones or more in general for aviation applications the gravimetric energy density has to be as high as possible; while for automotive applications the volumetric energy density is more interesting. For the three chemists these energy densities are calculated starting from the total electric energy defined in Eq. (3) for each C-rate and then averaged. The obtained gravimetric energy densities are 95.49, 212.85, and 220.28 Wh/kg respectively for LFP, NCA, and NMC cells; while the volumetric energy density are 210.29, 609.76, and 635.98 Wh/l respectively for LFP, NCA, and NMC cells. NCA and NMC cells have higher volumetric and gravimetric energy density than LFP battery. These cells are able to supply more electric energy than LFP at the same weight and occupied volume, and the NMC is the most performing considering these two parameters.

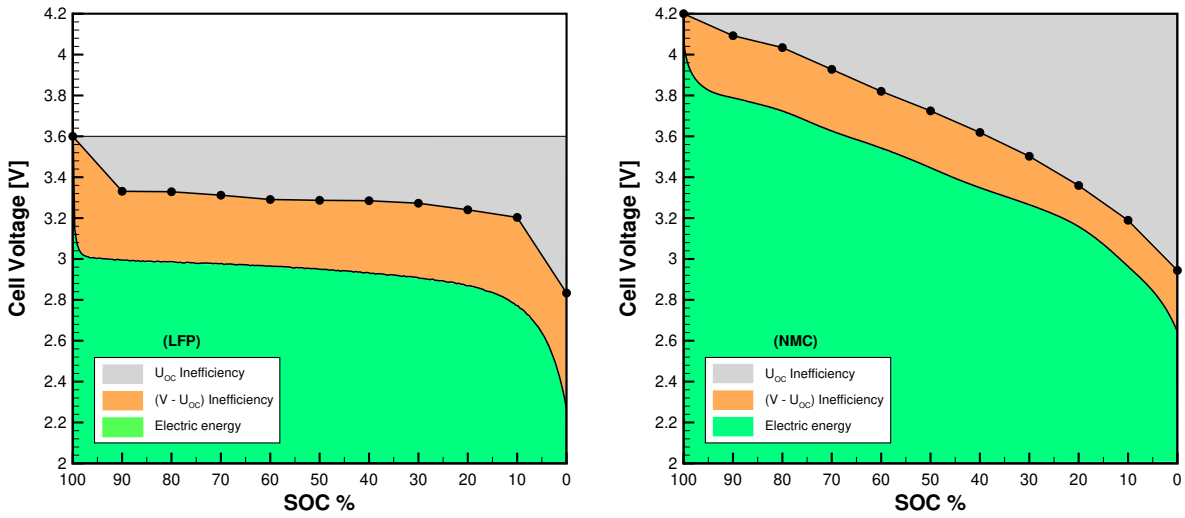

Fig. 10 Sources of inefficiency for NMC and LFP batteries.

6 Conclusions

This paper presented an experimental comparison of different chemists (LFP, NMC and NCA) of lithium-ion batteries. The focus is on the evaluation of the heat generation under different operating currents through a simplified equation, in which the different terms were experimentally quantified.
The main findings of the work can be summarized as follows:

- The cell voltage during the discharge phase can be considered almost constant between 90% and 10% SOC, for the LFP case, while shows a negative sloping evolution for the other two (NMC and NCA).
- The LFP is the one with the lowest temperature reached at the end of the discharge, but it is worth mentioning that for equal C-rate the actual current for the LFP is the lowest one. On the contrary, the NCA returned the highest temperature, and in fact already at 4C the cell was about the exceed the safety temperature. In addition, the IR thermography analysis showed that the NCA has the worst temperature uniformity
- The heat generated is higher in the NCA cell, which is also the one with the highest overpotential. The NMC is the intermediate case, while the LFP showed the lowest values despite the high overpotential. The latter in fact is compensated by a low current discharge.
- Accordingly, the NCA returned both the lowest energy efficiency and the highest ratio between heat generated and electric energy supplied. The NMC had a lower ratio than the LFP, but a similar efficiency as the decreasing voltage with SOC is not considered in the ratio.

The experimental methodology applied in this study can be used as a standard for future tests on other cell types. In addition, the obtained results in this study can be useful as input parameters for the design and optimization of different cooling strategies for batteries and for validation of future numerical methods.

Author Contributions

Luca Giammichele: Conceptualization (equal); Data curation (equal); Formal analysis (equal); Investigation (equal); Methodology (equal); Project administration (equal); Resources (equal); Supervision (equal); Validation (equal); Visualization (equal); Writing – original draft (equal); Writing – review and editing (equal). Daniele Colarossi: Conceptualization (equal); Data curation (equal); Formal analysis (equal); Investigation (equal); Methodology (equal); Project administration (equal); Resources (equal); Supervision (equal); Validation (equal); Visualization (equal); Writing – original draft (equal); Writing – review and editing (equal). Valerio D'Alessandro:Conceptualization (equal); Data curation (equal); Formal analysis (equal); Investigation (equal); Methodology (equal); Project administration (equal); Resources (equal); Supervision (equal); Validation (equal); Visualization (equal); Writing – original draft (equal); Writing – review and editing (equal). Matteo Falone: Conceptualization (equal); Data curation (equal); Formal analysis (equal); Investigation (equal); Methodology (equal); Project administration (equal); Resources (equal); Supervision (equal); Validation (equal); Visualization (equal); Writing – original draft (equal); Writing – review and editing (equal).

Conflicts of interest

There are no conflicts to declare.

References

1 M. Lowe, S. Tokuoka, T. Trigg and G. Gereffi, *Duke University Center on Globalization, Governance and Competitiveness, Tech. Rep.*, 2010.
2 E. Karden, S. Ploumen, B. Fricke, T. Miller and K. Snyder, *Journal of Power Sources*, 2007, **168**, 2–11.
3 T. Mller, Seventeenth Annual Battery Conference on Applications and Advances. Proceedings of Conference (Cat. No.02TH8576), 2002, pp. 113–118.

4 J. Speirs, M. Contestabile, Y. Houari and R. Gross, *Renewable and Sustainable Energy Reviews*, 2014, **35**, 183–193.

5 M. Wada, *Journal of Environmental Sciences*, 2009, **21**, 745–749.

6 H. de Wilde and P. Kroon, *ECN*, 2013, **ECN-E–13-005**,.

7 R. Matthe, H. Mettlach and L. Turner, *SAE International Journal of Engines*, 2011, **4**, 1944–1962.

8 A. Pesaran, S. Santhanagopalan and G. Kim, *Addressing the impact of temperature extremes on large format li-ion batteries for vehicle applications (presentation)*, National renewable energy lab.(nrel), golden, co (united states) technical report, 2013.

9 T. M. Bandhauer, S. Garimella and T. F. Fuller, *Journal of The Electrochemical Society*, 2011, **158**, R1.

10 K. Smith and C.-Y. Wang, *Journal of Power Sources*, 2006, **160**, 662–673.

11 C. R. Pals and J. Newman, *Journal of The Electrochemical Society*, 1995, **142**, 3282–3288.

12 Y. Chen and J. W. Evans, *Journal of The Electrochemical Society*, 1993, **140**, 1833–1838.

13 S.-C. Chen, Y.-Y. Wang and C.-C. Wan, *Journal of The Electrochemical Society*, 2006, **153**, A637.

14 Y. Chen and J. W. Evans, *Electrochimica Acta*, 1994, **39**, 517–526.

15 N. Nieto, L. Díaz, J. Gastelurrutia, I. Alava, F. Blanco, J. C. Ramos and A. Rivas, *Journal of The Electrochemical Society*, 2012, **160**, A212–A217.

16 B. Manikandan, C. Yap and P. Balaya, *Journal of The Electrochemical Society*, 2017, **164**, A2794–A2800.

17 L. Giammichele, V. D'Alessandro, M. Falone and R. Ricci, *Applied Thermal Engineering*, 2022, **205**, 117974.

18 M. Shadman Rad, D. Danilov, M. Baghalha, M. Kazemeini and P. Notten, *Electrochimica Acta*, 2013, **102**, 183–195.

19 G. Richardson and I. Korotkin, *Electrochimica Acta*, 2021, **392**, 138909.

20 M. Al-Zareer, C. Da Silva and C. H. Amon, *Journal of Power Sources*, 2021, **510**, 230362.

21 P. Qin, M. Liao, W. Mei, J. Sun and Q. Wang, *Applied Thermal Engineering*, 2021, **195**, 117212.

22 S. K. Mohammadian and Y. Zhang, *Journal of Power Sources*, 2015, **273**, 431–439.

23 H. Wang, T. Tao, J. Xu, X. Mei, X. Liu and P. Gou, *Applied Thermal Engineering*, 2020, **178**, 115591.

24 Y. Fang, F. Ye, Y. Zhu, K. Li, J. Shen and L. Su, *Energy Reports*, 2020, **6**, 238–247.

25 J. Duan, J. Zhao, X. Li, S. Panchal, J. Yuan, R. Fraser and M. Fowler, *Energies*, 2021, **14**, 4187.

26 L. Giammichele, V. D'Alessandro, M. Falone and R. Ricci, *International Journal of Heat and Technology*, 2022, **40**, 1 – 8.

27 Y. Liu, G. Aldan, X. Huang and M. Hao, *Applied Thermal Engineering*, 2023, **233**, 121184.

28 X. Duan and G. Naterer, *International Journal of Heat and Mass Transfer*, 2010, **53**, 5176–5182.

29 Y. Li, Y. Du, T. Xu, H. Wu, X. Zhou, Z. Ling and Z. Zhang, *Applied Thermal Engineering*, 2018, **131**, 766–778.

30 V. Talele, M. S. Patil, S. Panchal, R. Fraser and M. Fowler, *Journal of Energy Storage*, 2023, **65**, 107253.

31 Y. Gan, L. He, J. Liang, M. Tan, T. Xiong and Y. Li, *Applied Thermal Engineering*, 2020, **179**, 115740.

32 M. Chen and J. Li, *Journal of Energy Storage*, 2020, **32**, 101715.

33 L. Cattani, M. Malavasi, F. Bozzoli, V. D'Alessandro and L. Giammichele, *Energies*, 2023, **16**, 5071.

34 D. Bernardi, E. Pawlikowski and J. Newman, *Journal of The Electrochemical Society*, 1985, **132**, 5–12.

35 C. Forgez, D. Vinh Do, G. Friedrich, M. Morcrette and C. Delacourt, *Journal of Power Sources*, 2010, **195**, 2961–2968.

36 K. E. Thomas, C. Bogatu and J. Newman, *Journal of The Electrochemical Society*, 2001, **148**, A570.

37 F. Geifes, C. Bolsinger, P. Mielcarek and K. P. Birke, *Journal of Power Sources*, 2019, **419**, 148–154.

38 S. S. Madani, E. Schaltz and S. Knudsen Kær, *Energies*, 2019, **12**, 2685.